An injection head to generate a stable falling liquid film within a circular duct

Luis Borraz[a,b,*], Fernando Larrainzar[a], Florencio Sánchez-Silva[a], Ignacio Carvajal-Mariscal[a], Juan A. Reyes-Nava[b], Alberto Beltrán[c,*]

[a]*Laboratorio de Ingeniería Térmica e Hidráulica Aplicada, Instituto Politécnico Nacional, Unidad Profesional "Adolfo López Mateos", Zacatenco, Del. Gustavo A. Madero, C.P.29082, Ciudad de México, México*
[b]*Instituto de Investigación e Innovación en Energías Renovables, Universidad de Ciencias y Artes de Chiapas, Libramiento norte poniente No 1150, Col. Potinaspak, C.P. 29018, Tuxtla Gutiérrez, Chiapas, México*
[c]*Instituto de Investigaciones en Materiales, Unidad Morelia, Universidad Nacional Autónoma de México, Antigua Carretera a Pátzcuaro No. 8701, Col. Ex Hacienda de San José de la Huerta, C.P. 58190, Morelia, Michoacán, México*

1. Background

Different devices in the chemical, nuclear and energy industries use the liquid film flow as a medium of transport to carry out certain processes that cannot be achieved with any other type flow patterns. In particular, the liquid film flow is found in industrial processes of evaporation, distillation, film cooling, catalysis, among others [1, 2, 3]. This flow has great advantages due to its high sensitivity to fluid temperature, low flow residence times, low pressure drops in the ducts; as well as, high mass and thermal energy transport [4].

In this work, we present a new design of an injection head to generate a film of water in circular ducts, which was originally designed to protect the walls of an in situ downhole steam generator for oil applications. To confirm its good performance, the experimental and numerical analysis of the thickness and characteristics of the liquid film in interaction with 5 air jets was carried out, checking its stability and uniformity throughout the whole duct.

---
[*]Corresponding author
Email address: `laborrazj@gmail.com` (Luis Borraz)
Phone number: +52-967-147-2651

2. Head design

2.1. Hydraulic head design

The development of this new injection head was for an application of petroleum engineering although it is not limited to this field. For this specific case, the injection head was designed for an on-site steam generator that operates with rapid internal combustion at high pressures. One of the main problems with this system is the high temperature inside the combustion chamber. To protect the walls from these temperatures, an injection head was designed that generates a uniform water film, see Fig. 1. It was named as Down Hole Steam Generator ($DHSG$) [5]. The combustion chamber of the $DHSG$ has an outer pipe diameter D_t of 101.60 mm and 1.00 m in length L_p.
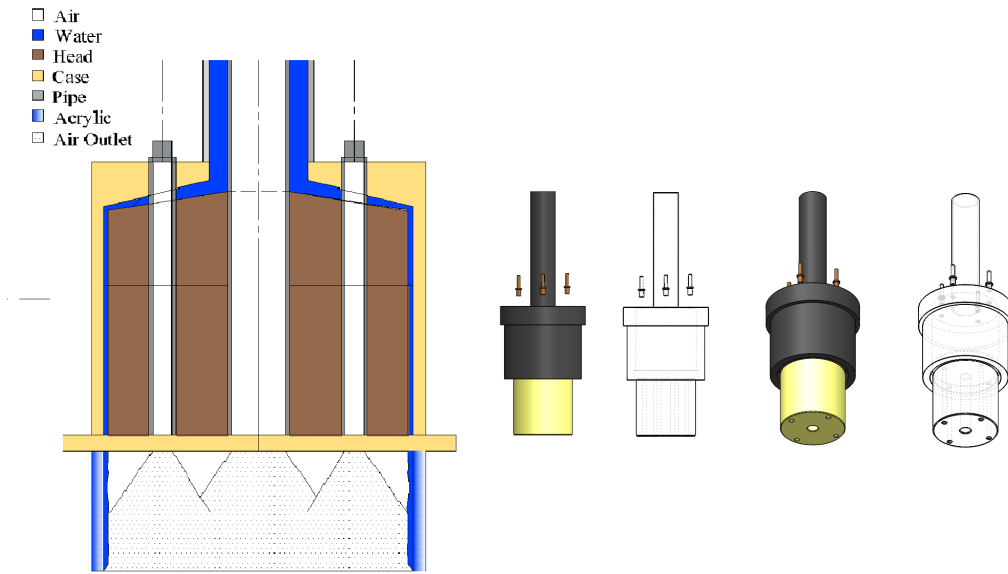

Figure 1: $DHSG$ injection head, from left to right and from top to bottom: Cut plane and isometric views. Dimensions of the DHSG head with water and air injectors, cut plane view. Hydraulic injection head design, annular geometry at the head outlet, inverted cone geometry and compensated inclined plate. The pipe of greater diameter (chamber) is not included in the figures.

The injection head consists of a inclined plate at 10 ° [6] that distributes the liquid to generate the film from an annular duct (pipe with a smaller

diameter) towards the combustion chamber (pipe with a larger diameter) as shown in Fig. 1. It also has four smaller concentric nozzles (ϕ=5.86 mm) for the injection of oxygen (O_2), an a central one (ϕ=16.60 mm) for the injection of methane (CH_4) and a central nozzle for injection of water and its subsequent atomization. All these elements together are intended to generate steam [7]. It is important to mention that neither the combustion of methane nor the atomization of the central jet water is included in the experimental installation for this study. In such a way the study is limited to the interaction of the water film with 5 air jets in the system (head-pipe) in order to analyze the dynamics of the system described in Fig. 1.

The water mass flows $\dot{m}_w$ to form the liquid film, according to the requirements of $DHSG$ [6], were in the range of 0.62-0.75 kg/s and corresponds to Reynolds film numbers in the range of $8,340 \leq Re_{w,f} \leq 10,088$ 1. With the equation of Wang et al. [8] and the maximum water flow corresponding to 0.75 kg/s of this research, it is possible to estimate the liquid film thickness δ as:

$$\delta = 626(Re_{w,f}^{0.424})(\frac{\nu_w^2}{g})^{\frac{1}{3}} \tag{1}$$

where $Re_{w,f}$ is the Reynolds liquid film number of the water that is defined as:

$$Re_{w,f} = \frac{4\dot{m}_w}{\pi D_h \mu_w} \tag{2}$$

ν_w and μ_w are the kinematic and dynamic viscosity of water, respectively. g is the acceleration of gravity, D_h is the hydraulic diameter of the chamber with a value of ϕ=94,66 mm. The resulting $Re_{w,f}$ was 10,088 and the theoretical liquid film thickness δ was 1.46 mm. This δ was used to define the liquid outlet dimensions from the head to the chamber 1. The head that discharges the liquid into the chamber has a liquid inlet and an annular outlet also shown in 1 with an area of $A_{cs,annulus}$=427.47 mm^2.

It is taken as a principle to keep the cross-sectional area $A_{cs,annulus}$ along the passage of the liquid towards the inner part of the chamber as shown in the Fig. 1. This is to keep the average velocity of the liquid constant throughout the injection head so that it can be supplied in a smooth and uniform way. Although the nature of the water flow is turbulent from the inlet, the injection will be without great disturbances, seeking that the ve-

locity profile does not change abruptly before leaving towards the walls of the $DHSG$ where the liquid film will be generated 1.

This injection head has a connection with an umbilical tube, which allows the inclusion of the feeding water-air tubes 1. It is attached to the chamber of the $DHSG$ by means of a weld neck flange. The diameter of the oxygen injection nozzle was 16.60 mm, while for methane it was 5.86 mm. For this device, a 134.00 mm casing was designed, which served as a protection for the injection head, where the lines for feeding fluids are connected mentioned above, as well as in the conduits through which water circulates for the formation of the liquid film.
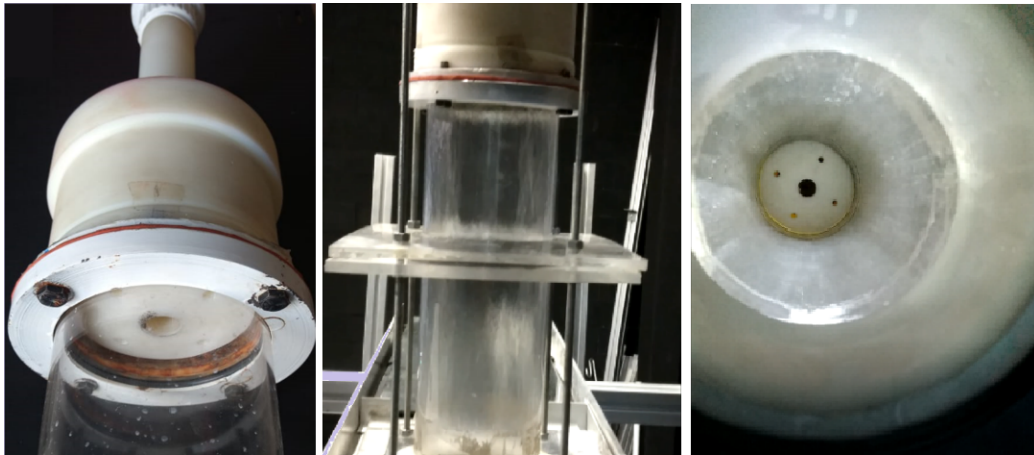

Figure 2: Injection head coupled to an acrylic pipe of 101.6 mm outside diameter.

The assembly is machined in Nylamid, the flanges are made of steel $SA - 515$ Grade 70 and the connections are based on screws. The system is composed of an acrylic tube of 101.60 mm in outer diameter and 1.00 m in length, as a result is that the straight section of the head is equal to 25 annular hydraulic diameters according to the previous section. With these conditions and the capacity of the air accumulator tank, the system will be able to maintain stable conditions for experimentation in two-phase flow in the film flow pattern for 2 min [9].

2.2. Air and water supply section

This section consists of a 10 HP positive displacement air compressor, conformed of an accumulator tank that handles a maximum pressure of 1,379

kPa at a temperature of 232 K. However, the tank is calibrated at a pressure of 896.35 kPa. Subsequently, the air is conducted through a 12.70 mm diameter pipe to the section that divides the mass flow into 5 flows, the division is 4 times the same physical flow that is supplied to the four nozzles for air injection and the fifth air flow is supplied in the center of the head 1. The water supply section consists of a water tank with a capacity of 0.45 m^3 (450 l) and a 1 HP centrifugal pump. The water is led to the measuring section by means of a 19.00 mm PVC pipe [9].

3. Experimental facility

All the experiments were performed maintaining steady flow conditions inside the vertical pipe (chamber) of the $DHSG$. The diagram of the experimental device of this study is shown in the figure 3, it is basically made up of an acrylic tube of 1.00 m long, 95.60 mm internal diameter and a pipe thickness of 3.00 mm.
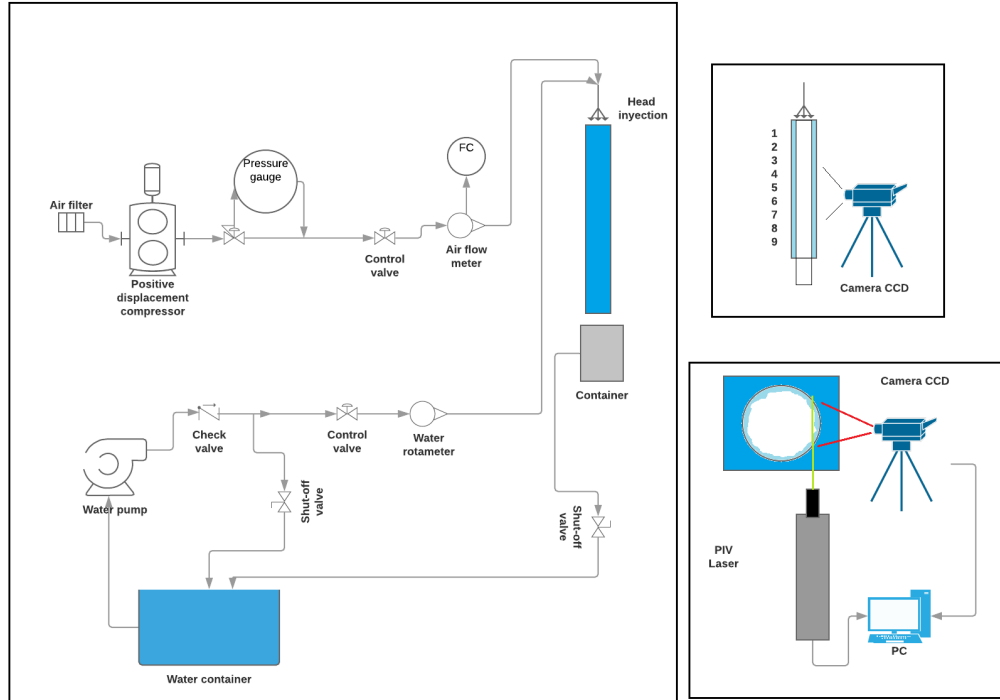
Figure 3: 1- Filter: 2- Air compressor; 3- Accumulator; 4- Measuring system Air; 5- Experimental visualization setup ; 6- Water tank; 7- Pump; 8- Measuring system Water; 9- Water inlet; 10- Return of water; 11- Phases separator; 12- Airflow inlet; 13- Acrylic Box; 14- Camera CCD; 15- Axial observation area; 16- Optical correction tank; 17- Liquid with particles; 18- Laser light of PIV; 19- PIV. [9].

The display section of the laser was located from 22 cm (0.19 D_t) below the injection point, up to 45 cm (4.5 D_t), to observe the development of the flow. Although flow velocity profiles are expected to be fully developed at this distance from the inlet, it is known from works by Webb and Hewitt [10] that these flows continue to evolve along the pipeline. An arrangement was made in the display section to match the refractive indices of water, air and wall in the line of sight of the optics measurement.

3.1. Operating procedure

The velocity fields of the water film were obtained using a non-intrusive optique technique called Particle Image Velocimetry (PIV). Figure 3 shows a diagram of the arrangement of the elements in the experimentation zone.

The system uses a *Neodymium* double head laser made by the company *Litron Laser*; model LDY 303 HE PIV. The scattered light was recorded using a high-speed camera with a Charge Coupled Device (CCD) placed at 90° with respect to the light curtain generated by the laser, as illustrated in figure 3. The displayed area was 50 by 30 mm, which corresponds to a spatial resolution of 1632 by 1200 pixels. During each measurement of the fields of the liquid film, a set of 400 pairs of images were taken at a frequency of 100 Hz. The raw images in the PIV were converted to binary images (gray scale) with the help of an image recognition algorithm made in $MATLAB$ [9]. Through the calibration of a threshold, the water-air interface and the internal wall of the pipe were identified, which subsequently allowed determining the instant axial liquid film thickness, as well as its average [11]. A sweep was made along the pipe, taking data every 50 mm from zone 1 to zone 9, see Fig. 3, covering a total of 450 mm. The total average film thickness and the total average velocity of the film were calculated. Figure 4 shows the sequence of the processing of the images that allows determining the parameters of interest 4.
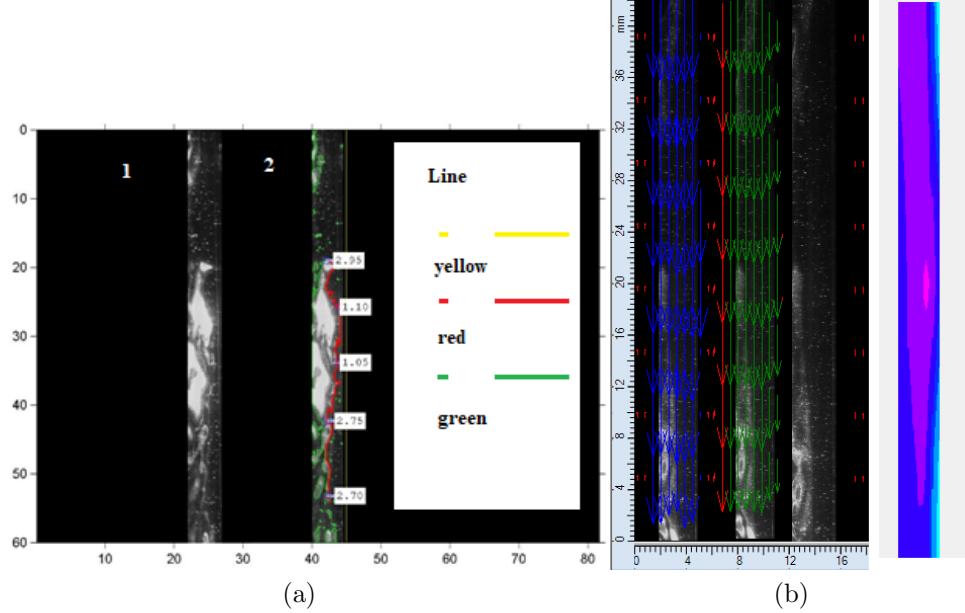

(a)　　　　　　　　　　(b)

Figure 4: Liquid film thickness measurement by morphological recognition, from left to right: image unprocessed, image processed and filtered velocity vectors.

7

Left image in Fig. 4a is a rough photograph of the falling liquid film where bubbles, glitters, the liquid-gas interface and the pipe wall (rightmost) can be seen. The right image 4b is a photograph processed with the algorithm where the yellow line on the far right represents the wall of the pipe, the red line is the detected interface and the green line is detected information that is not required for the liquid film thickness measurement. The analysis of the images obtained was carried out with the software package of $DynamicStudio$ v3.20. Initially the images were preprocessed for the Signal-to-Noise Ratio (SNR). The calculation of the velocity fields were carried out using a multi-step cross-correlation algorithm [9]. The PIV window or PIV mesh was first set to 32 by 64 pixels. The calculation of the average velocity of the liquid film was made by tracking the displacement of each particle, from one image to another, producing the velocity vectors of the liquid film. Finally, the instantaneous vector maps were time averaged and the wrong vectors were eliminated using a criterion based on a range of velocity permissiveness and a filtering called "average filter". The time-averaged and filtered velocity fields were also spatially averaged to obtain velocity profiles within the falling water film.

4. Numerical model

In order to model the liquid film flow, it was necessary to solve the conservation equations of the fluid dynamics in the computational domain shown in Fig. 5. In this research, the solver $interFOAM$ was used, which allows the modeling of two or more immiscible fluids [12]. It uses a tracking technique that captures the interface between the interacting phases. This powerful tool allows the simulation of the free surface of complex flows with an arbitrary shape in any situation and is capable of modeling the rupture or union of phases [13]. It is even possible to model the transfer of heat and mass through the interface by solving additional energy and mass transfer equations, which were not used in this study. The formulation is based on the fact that two or more fluids (or phases) are not interpenetrated. In this model, the resolution of a single set of equations for the conservation of the mass and the momentum was carried out by sharing the resulting velocity field between the phases. The volumetric fraction of each of the phases was solved with an additional transport equation, from which it is possible to define the position and evolution of the interfaces. The biggest problem that this model must solve is precisely the calculation of the interfaces that delimit each of

the phases within the domain [13]. The fields of all the variables (velocity, pressure) are shared by all the phases and represent averaged values based on the volumetric fractions of each one of them.

For the numerical model that describes the interaction of the liquid film with the air jets it is assumed the following:

- Transient 3D flow of the two fluids (water, air);

- Turbulent flow fully developed at the entrance;

- Flow in two phases incompressible and adiabatic;

- Properties of constant fluids;

Compressibility effects are not considered in the model since the Mach M_a number for all flows in this study are low. The continuity and momentum equations (Navier-Stokes equations) of the $interFOAM$ solver coupled to a turbulence model $LES\ k-equation$ were solved in the computational domain to predict velocity and pressure fields [14]:

$$\nabla \cdot \underline{\bar{u}} = 0, \tag{3}$$

$$\rho \left[\frac{\partial \underline{\bar{u}}}{\partial t} + \nabla \cdot (\underline{\bar{u}}\underline{\bar{u}}) \right] = -\nabla \bar{p} + \rho \underline{g} + \mu \nabla \cdot (\nabla \underline{\bar{u}}) + \nabla \cdot \underline{\underline{\tau}}^{sgs} + \underline{f}_{surf}, \tag{4}$$

where $\underline{\bar{u}}$ is the spatially filtered velocity vector, $\bar{p}$ the spatially filtered pressure, $\underline{\underline{\tau}}^{sgs}$ is the subspace turbulent stress tensor, $\underline{f}_{surf}$ is the source term for surface tension and $\underline{g}$ represents the gravitational field. From a mathematical point of view, the LES techniques employ spatial averaging of the transport equations using a filter of size Δ that serves as a boundary between the macroscales to be solved and the microscales to be modeled [13].

In the $LES\ k-equation$ model, eddies with scales of small length are spatially filtered before the application of the Navier-Stokes equations, while larger eddies are solved according to the Kolmogorov scales [13]. Subsequently, the smaller eddies are modeled using the mesh subscale closure (sgs). For turbulent closure, the conservation of turbulent kinetic energy is:

$$\frac{\partial \rho k}{\partial t} + \nabla \cdot (\mu_{eff} \nabla k) - \rho \underline{\underline{\tau}}^{sgs} : \underline{\underline{S}} - C_e \rho \frac{k^{\frac{3}{2}}}{\Delta}, \tag{5}$$

9

where $\underline{\underline{S}}$ is the strain rate tensor. The term $\underline{\underline{\tau}}^{sgs} : \underline{\underline{S}}$ corresponds to the rate of production of turbulent kinetic energy, while $C_e \rho \frac{k^{\frac{3}{2}}}{\Delta}$ is the term responsible for the rate of dissipation of this energy [15]. The subgrid stress tensor $\underline{\underline{\tau}}^{sgs}$, is modeled using the Boussinesq approximation [15]:

$$\underline{\underline{\tau}}^{sgs} = -2\mu^{sgs} dev(\underline{\underline{S}}) + \frac{2}{3}\rho k I; \quad dev(\underline{\underline{S}}) = \frac{1}{2}[\nabla \underline{u} + (\nabla \underline{u})^T], \qquad (6)$$

and the mesh subscale viscosity μ^{sgs} is calculated according to [16]:

$$\mu^{sgs} = \rho C_v \Delta \sqrt{k}, \qquad (7)$$

where the constants C_v and C_e are equal to 0.094 and 1.048. For more details of this turbulence model, see Zamorano [15].

In the VOF model, the conservation of the volume fraction is solved in an additional equation by:

$$\frac{\partial \bar{\alpha}}{\partial t} + \nabla \cdot (\bar{\alpha}\underline{u}) + \nabla \cdot (\underline{u}_r \bar{\alpha}(1 - \bar{\alpha})) = 0, \qquad (8)$$

where the volumetric contributions of each phase can be added ($\bar{\alpha}$ represents the volumetric fraction of the primary phase (liquid) and can take values from zero to unity). In interFOAM, the properties of fluids on the momentum equation 4 are defined according to the following [14]:

$$\rho = (1 - \bar{\alpha})\rho + \bar{\alpha}\rho \qquad (9)$$
$$\mu = (1 - \bar{\alpha})\mu + \bar{\alpha}\mu \qquad (10)$$

The fields for all variables and properties are shared by the phases and represent averaged volume values, as long as the location of the volumetric fraction $\bar{\alpha}$ of each of the phases are known. Therefore volumetric fractions can have the following conditions:

- $\alpha = 0$: The cell is empty (from the primary water phase).

- $\alpha = 1$: The cell is full (from the secondary phase)

- $0 < \alpha < 1$: The cell contains the interface between the primary phase (water) and the secondary phase (air).

The effect of surface tension along the interface is considered and is entered into the solver with a constant value of $0.072 \ N/m$. Its effect is induced in the source term $\underline{f}_{surf}$ as a body force where it is modeled according to the method CSF (Continuous Surface Force) of Brackbill et al . [17].

4.1. Geometry, boundary conditions, meshing and numerical schemes

The geometry of the numerical model is based on the experimental arrangement described in section 3. Figure 5 shows the computational domain. The mesh length was 1.00 m downstream of the injection head, to capture the interface and quantify the liquid film thickness throughout the domain. Due to the interaction between the air jets and the liquid film generates turbulent anisotropic eddies within the chamber, a three-dimensional geometry was chosen in order to capture these effects. The computational domain is limited by the water inlet, 5 air inlets, head walls, chamber walls and the outlet.
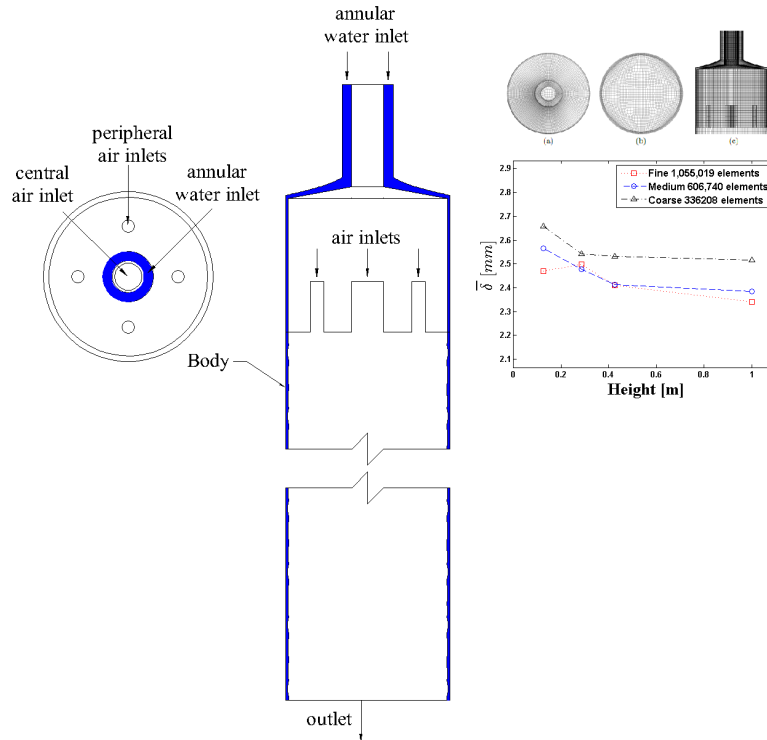

Figure 5: Computational domain, from left to right: Water and air inlets, body and outlet. For the internal volume: a) inlets, b) outlet, c) body. Mesh sensitivity analysis for the average water film thickness $\bar{\delta}$ at different heights for the 16 test number. Numerical results for the case with higher water-air flows.

The Reynolds number for the air and water inside the injection head is equal to:

11

$$Re_* = \frac{D_h \, u_{in}}{\nu} \tag{11}$$

where u_{in} is the injection velocity of the phase and D_h is the hydraulic diameter. On the inlet of water, D_h was equal to the hydraulic diameter of an annulus. The hydraulic diameter at the air inlet D_h was equal to the sum of the internal diameters of the nozzles.

It was induced in the pipe that represents the chamber of the $DHSG$, flows of water and air in an interval of $Re_{w,c}=$ 16,046-19,366 for the central annulus, $Re_{a,c}=$ 3,784-32,177 in the central nozzle and $Re_{a,p}=$ 2,688-22,845 in the peripheral nozzles, where the chamber is at a pressure with an interior of 78,300 Pa (local pressure) and a constant temperature of 288 K, all according to the conditions and the experimental mass flows 1.

| Test Number | Water Inlet (Total Area = 4.27×10^{-4} [m^2]) | | | | Air Inlet (Total Area=3.24×10^{-4} [m^2]) | | | | | | |
	Mass Flow $\dot{m}_w$ [$\frac{kg}{s}$]	Average Velocity Inlet $U = (0, -v_{in,w}, 0)$ [$\frac{m}{s}$]	Reynolds Number $Re_{w,c}$	Turbulent Intensity I_{turb} [-]	Manometric Pressure P_m [$\frac{kgf}{cm^2}$]	Average Velocity Inlet [$\frac{m}{s}$] $U = (0, -v_{in,a}, 0)$		Reynolds Number Re_a		Turbulent Intensity I_{turb} [-]	
					Without Air Flows Injection						
1	0.62	1.45	16046	0.05							
2	0.66	1.54	17042	0.05							
3	0.70	1.64	18148	0.05	0.00						
4	0.75	1.75	19366	0.05							
		With Air Flows Injection				Central	Peripheral	Central	Peripheral	Central	Peripheral
5					0.80	3.45	6.93	3784	2688		
6	0.62	1.45	16046	0.05	2.00	12.94	25.97	14191	10079	0.05	0.05
7					3.40	29.34	58.87	32177	22845		
8					0.80	3.45	6.93	3784	2688		
9	0.66	1.54	17042	0.05	2.00	12.94	25.97	14191	10079	0.05	0.05
10					3.40	29.34	58.87	32177	22845		
11					0.80	3.45	6.93	3784	2688		
12	0.70	1.64	18148	0.05	2.00	12.94	25.97	14191	10079	0.05	0.05
13					3.40	29.34	58.87	32177	22845		
14					0.80	3.45	6.93	3784	2688		
15	0.75	1.75	19366	0.05	2.00	12.94	25.97	14191	10079	0.05	0.05
16					3.40	29.34	58.87	32177	22845		

Table 1: Experimental and numerical flows.

For the numerical model, a hydrostatic pressure condition was used at the outlet with a differential pressure between the inlet and the outlet of $\Delta P_h = 0$. The volumetric fraction at the inlet was constant with a value α_w = 1, which means that only water enters, while the volumetric fraction of air at 5 nozzles was also constant with a value α_w = 0, meaning only air inlet 2.

In combination with the water velocity inlet boundary condition, a fluctuating turbulent inlet boundary condition was used to disturb the flow and thereby be able to generate the disturbance waves that appearing in the annular flow [18]. This boundary condition generates small fluctuations when adding a random component to an average reference field, in this case the velocity v_{in}:

$$v_{in,w,rand} = (1 - \alpha_r)(v_{in,w,ref}^{n-1}) + \alpha_r[v_{in,w,ref} + (s)(C_{rms})(v_{in,w,ref})] \qquad (12)$$

where $v_{in,w,rand}$ corresponds to the value of the field at the new instant, $v_{in,ref}$ is the reference value of the patch, n is the time step, α_r is the faction of the new random component added to the previous value in time, C_{RMS} is a coefficient of the root mean rms and s is the fluctuation scale. This function has two control parameters, and the value used for α_r and for s was 0.1 respectively. In all simulations, water was selected as the primary phase and air as the secondary phase, however, the results are not affected by the selection of water as the primary phase [19]. The properties of the fluids were corresponding to those of the experiment according to the conditions of temperature and local atmospheric pressure. The properties of air and water were constants with next values: $\mu_w = 1.51 \times 10^{-5}$ and $\mu_a = 1.51 \times 10^{-5}$ m^2/s, $\rho_w = 1.21$ and $\rho_w = 998.00$ kg/m^3 and a surface tension σ of 0.072 N/m respectively.

Turbulence intensity levels at the inlets were not measured in the experiment. So they were approximated in the simulations using 13 equation [13]:

$$I_{turb} = 0.16Re_* \ D_h^{-1/8} \qquad (13)$$

The non-slip boundary condition $v_{body} = 0$ was used in all the walls with a roughness of $\epsilon = 2 \times 10^{-5} m$. The initial conditions in the simulation were selected based on the experimental conditions. For the 4 cases of the film without air injection at t = 0 s the tube is full of air and when the water injection begins the air in the walls moves. For the 12 cases of the simulations with air injection at $t = 0 \ s$, we have the chamber with the liquid film already generated. These are achieved by mapping the scalar and vector fields with $OpenFOAM$ of the solution of the first case without air injection at $t = 5 \ s$. Subsequently, the air is injected into the nozzles with their corresponding velocity. This is done for the 12 cases with air injection to accelerate the convergence and to study the transient flow. The numerical schemes and details used in OpenFOAM are on the next table:

Discretization		Term	Scheme
Temporal		$\frac{\partial}{\partial t}$	Euler
Spatial	Gradient	∇u	Gauss linear
Spatial	Gradient	∇p	Gauss linear
Spatial	Divergence	$\nabla \cdot (\rho \phi u)$	Gauss upwind
Spatial	Divergence	$\nabla \cdot (\phi \alpha)$	Gauss vanLeer
Spatial	Divergence	$\nabla \cdot (\phi_{rb} \alpha)$	Gauss upwind
Spatial	Divergence	$\nabla \cdot (\tau_{ij})$	Gauss linear
Spatial	Laplacian	$\nabla \cdot (v \nabla u)$	Gauss linear corrected
Boundary conditions	$\bar{\bar{u}}$	$\bar{p}$	α
Inlet	$U = (0, -v_{in,w}, 0)$ $s = (0, -0.1, 0)$ $\alpha_r = 0.1$	fixedFluxPressure	$\alpha = 1$
Inlet2	$U = (0, -v_{in,a}, 0)$	fixedFluxPressure	$\alpha = 0$
Inlet3	$U = (0, -v_{in,a}, 0)$	fixedFluxPressure	$\alpha = 0$
Outlet	inletOutlet	prghPressure	$\nabla \alpha = 0$
Body (walls)	$U = (0, 0, 0)$	zeroGradient	$\nabla \alpha = 0$
Mesh resolution	$\Delta x_{max} = 3~mm, \Delta x_{min} = 1~mm, \Delta x_{wall} = 0.1~mm$		
Time step	$\Delta t_{initial} = 1.0 \times 10^{-6}~s$ and adjustable runtime		

Table 2: Numerical Schemes. Adapted from Neumman [14].

An structured mesh was used in this study to provide the best mesh quality using the $O - Grid$ 5 meshing strategy. A high-quality mesh was generated in the region near the wall to capture the water-air interface and to study the characteristics of the liquid film throughout the chamber. The mesh was done with $ANSYS~ICEM~CFD~v$19.1 software on a structured block domain 5. To determine the adequate mesh density, a mesh sensitivity analysis with 3 different densities was performed, doubling the number of cells for each case. Initially a coarse mesh was created such that at least six mesh points near the wall capture the liquid film interface near the walls on the radial direction. This requires a finer mesh in the region of the interface to capture the characteristics of this phenomenon in the simulation. Three adaptations were made 5. It was found that with a mesh of approximately 1×10^6 cells the results did not vary by more than 8% of the value of $\bar{\delta}$.

5. Results

5.1. Liquid film thickness distribution

For tests 1-4, the water falls under the influence of the gravitational field generating waves at the interface 6. When the water flows inside the chamber

that is initially filled with air, a non-fixed interface is generated between these two fluids, where also the difference in densities generated ripple waves on the liquid film according to Kelvin-Helmholtz instabilities. Even with very low $Re_{w,f}$ the liquid film was not smooth, but the wave movements were periodic. The observed waves were widely spaced, with long depressions between each one and small waves of capillary size following the peaks similar to those of the annular flow [18].
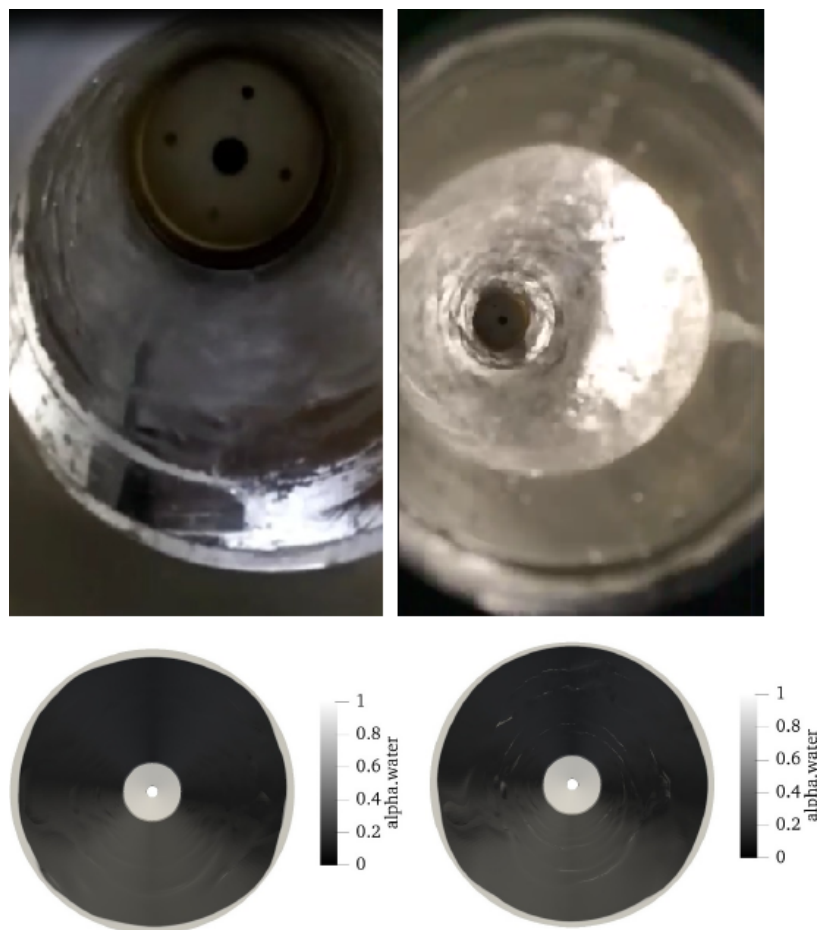

Figure 6: Perturbation waves on the water-air interface [18]. Tests 4 and 16. Isocontours of volumetric fraction α, from left to right: tests 4 and 16. The perturbation waves are show [18].

For intermediate mass flows of $\dot{m}_w$ and $\dot{m}_a$ (test 5-16), periodic movement was only observed near from the centered area; downstream, the periodic motion is replaced by a larger wave motion of higher frequency. The wave fronts were accompanied by smaller waves that were no longer capillary in size. When the flows of $\dot{m}_w$ and $\dot{m}_a$ went even more high, the flow became very complex and random. Numerically this behavior was similar, as can be seen in the figure 6 where we observe greater undulation at the interface (α=0.5) when air is injected.

The distribution of the water film thickness δ is reported here. The data of the average liquid film thickness $\bar{\delta}$ for the simulation and experimental correspond to the average of the points measured along the chamber. The harmony that exists between the experimental and numerical results is presented below. The results show that, for tests 1-4, the numerical and experimental thickness $\bar{\delta}$ have the same trend, being more similar for the design flow. In the experimental tests it was observed that the liquid film presents less undulation for the design flow, which is reflected in its greater stability. The gas-liquid interface became more uniform (fewer peaks) due to increased water flow.

The figure 7 is a graph of the position of the 16 sensors distributed uniformly to capture the interface and calculate the average liquid film thickness in simulation at different heights. This strategy was used in all cases. The central lines correspond to each axial position studied along the circular duct. The right image is an enlarged (zoomed) position of sensor number 15. The red line is the internal diameter of the pipe, and the other lines plotted correspond to the average liquid film thickness $\bar{\delta}$ which varies according to the axial position.
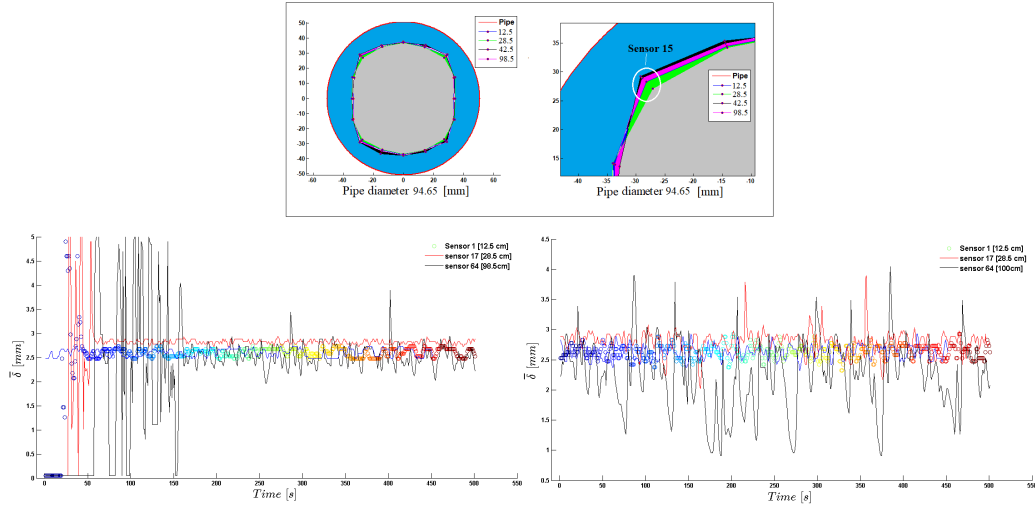
16

Figure 7: Sensors strategy to measure $\bar{\delta}$, from left to right: position of the 16 sensors and zoom of the sensor number 15. Test 1. Signal of water film thickness fo sensor 1, 17 and 64. Test 1. Signal of water film thickness for sensor 1, 17 and 64. Test 7.

Experimentally, it was observed that the water flow affects the stability of the liquid film, the higher the water flow shows a favorable effect on the formation of the liquid film, since the greater amount of movement of the water helps to isolate the undulations of the film making it more stable. Results in Fig. 8 show that, for tests 1-4, the numerical and experimental thickness $\bar{\delta}$ have the same trend, being more similar for the design flow. In the experimental tests it was observed that the film presents less undulation for the design flow, which is reflected in its greater stability. The gas-liquid interface became more uniform (fewer peaks) due to increased water flow. The results of the 16 cases studied in the numerical simulation are shown in figure 8. The length of the circular duct is on the axis of the abscissa, the first plotted point corresponds to 12.5 cm distance from the water outlet of the injection head and the end point is 1 m away from the injection of water. In the axis of the ordinates we have the average film thickness $\bar{\delta}$ of the 16 sensors for each axial position.
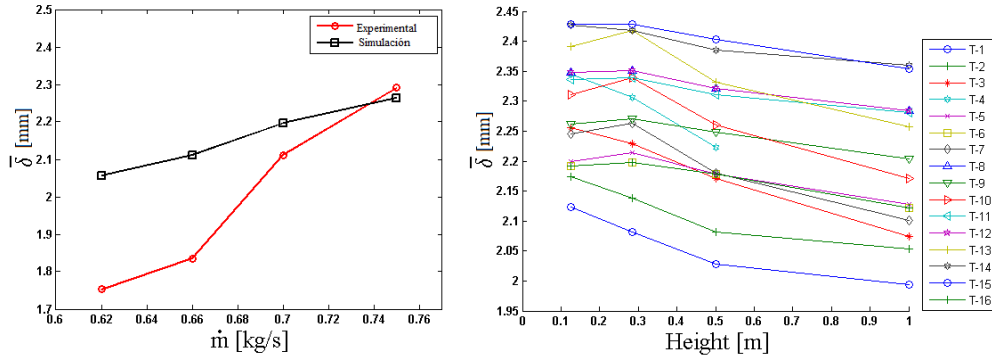
17

Figure 8: Left comparison of average water film thickness $\bar{\delta}$ between experimental and numerical analysis. Tests 1-4. Right average film thickness $\bar{\delta}$. Test 1-16.

In principle, the liquid film thickness is greater if the mass flow is greater. Visually and numerically at 30 cm the film thickness begins to be disturbed, due to the effect of gravity and the loss of kinetic energy. In the results with the air jets (test 5-16) interacting with the film, it was observed that the thickness of the film in the chamber decreases and has the same tendency of having the thicker when they are closer to the injection head and less when it is further away from the injection head, that is, downstream. This means that the liquid film was able to withstand air jets. It is also important to mention that this decrease in liquid film thickness is small compared to the average value $\bar{\delta}$ and adequate to maintain the protection of the walls of the $DHSG$.

All of the above is more clearly seen by studying the transient behavior of the film thickness $\bar{\delta}$ for the different axial zones in the 5 seconds of simulation. For example for cases 1-4, graph 7, the time against thickness $\bar{\delta}$ for three axial distances and the same water flow of 0.62 kg/s without air injection. The signal from sensor 1 presents a minimum ripple at zero time until a maximum disturbance at 0.44 s and this is due to the time it takes for the water to reach the sensor and homogenize the film around the inner duct. For sensor 17 the arrival time is approximately 0.60 s and presents a greater magnitude in thickness and less with respect to sensor 64. This last sensor, being further away, a ripple can be observed excessive and an average in its thickness less than the two referenced sensors.

For tests 5-16 the behavior of the liquid film is disturbed by the action of the air jets. In the figure 7 right side,there is a plot with the same charac-

18

teristics as the previous one,but with the difference of plotting case 7, which is injection of 0.62 $\frac{kg}{s}$ of water and injection of air. In this case, the filling of the water film is not shown, because once the internal part of the chamber is covered with the water film, the air is injected through the 5 ducts. The liquid film is mostly disturbed by the shear action of the air. It presents a greater amplitude with respect to test-1.

Another important effect of the air jets was a $shear zone$ generated, which occurs at 30 cm, being a critical zone since this flow pattern was characterized by a centralized gas core that can release liquid droplets entrained from the flowing liquid film. Knowledge of this cutting zone is essential for the proper design of $DHSG$, predicting the onset of dry heat flow (CHF) in boiling heat transfer, and cooling efficiency from the reactor core. In this critical zone, the cutting action of the combustion gases is more likely to atomize the water film, not in its entirety, but if they affect the mass balance and heat transfer between the hot gases and the walls of the $DHSG$. Next, figure 9 shows the difference in the trend in the film thickness curve when there is no air injection (test-4) and when there is it (test-16).
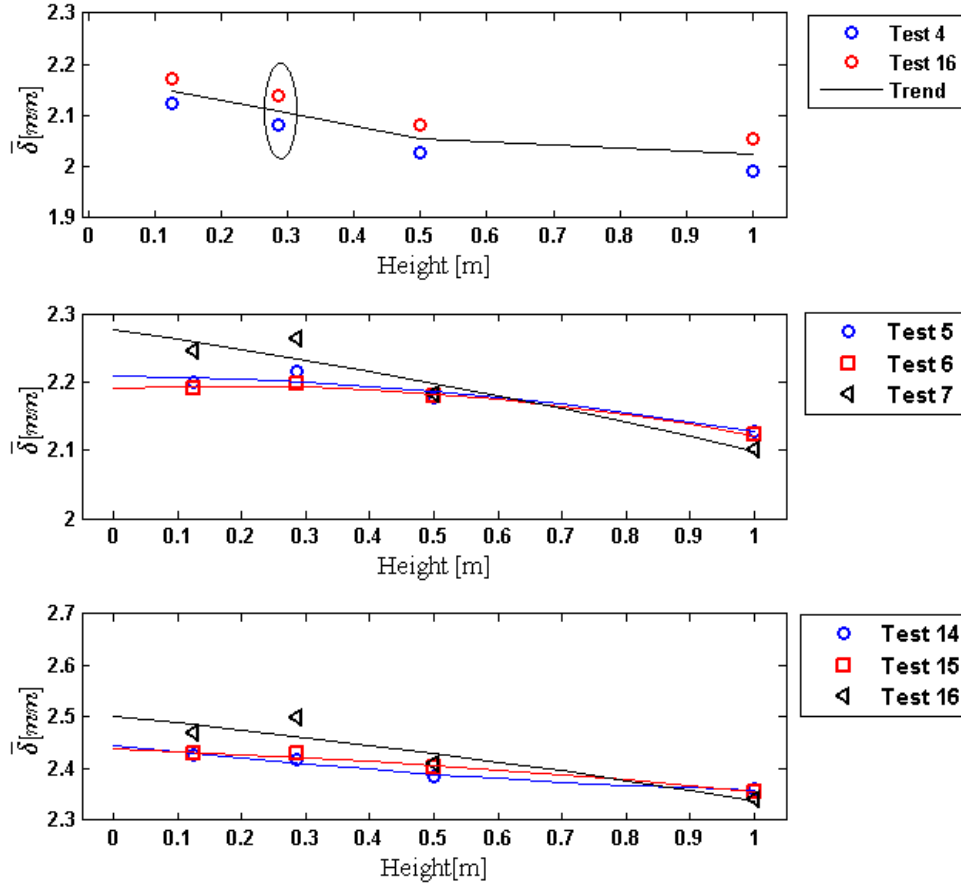
Figure 9: Impact of the perimeter air jets on the water liquid film. Test 4 and 16. Impact of the central air jet on the water liquid film. Test 5-7. Impact of the central air jet on the water liquid film. Test 14-16.

In the ellipse marked on the graph 9 shows the effect of the air due to the cone-shaped-jets opening of its, generating ridges in the liquid film resulting in a greater thickness. In this zone droplet entrainment from liquid film breakage can occur when a large shallow disturbance wave becomes steep along the direction in the gas flow core and forms a spike that can break into droplets. This behavior in the zone of greatest disturbance is true for others cases with air injection. However, at no time was the total breakdown of

20

the liquid film reached or leaving some area of the chamber dry, that is, the stability of the liquid film is optimal for the conditions studied.

Below, in figure 9 a graph of tests 5, 6 and 7 is presented, corresponding to the lowest water flow studied of 0.62 $\frac{kg}{s}$ with the interaction of air in three cases (test 5-7) 1.

This graph shows that air injection generates a significant cutting effect on the structure of the film, making it more wavy at 30 cm, as seen in previous cases. In the central part, the three lines converge at one point, making their linear decrease in the film thickness. These have to do with the penetration of the central jet which is the one with the greatest impact and its diffusion is almost in the middle of the water chamber. The same trend of the graph is presented for the case of design 1.75 kg/s. In figure 9 shows the behavior in tests 14, 15 and 16.

The same trend is also observed as in the previous cases. Concluding that the perimeter jets impact almost $30cm$ and the central jet 50 cm from the chamber. The validation of the film thicknesses is presented below. 10 The PIV and numerical results are as follows for all cases.
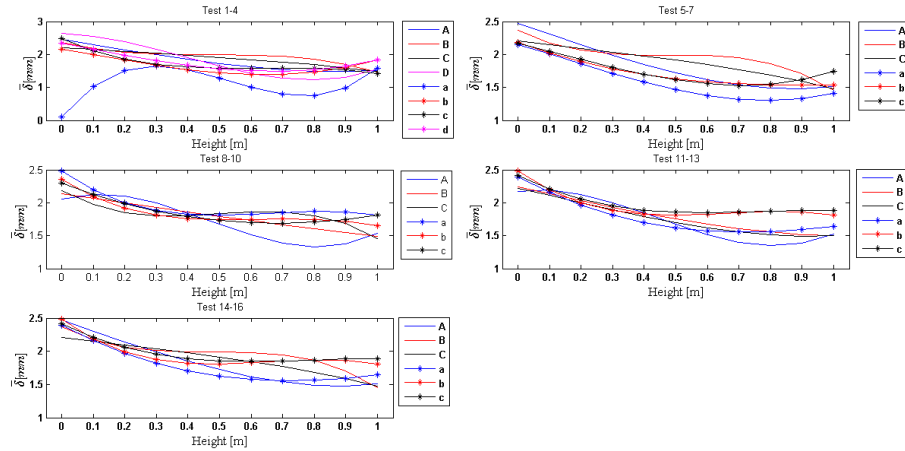

Figure 10: PIV (upper) and numerical (lower) liquid film thickness when there is no air flow. Tests 1-4. When there is air flow. Tests 5-7. Tests 8-10. Tests 11-13. Tests 14-16

In the 5 graphs of the figure 11, the capital letters in the legends represent the results of the film thickness obtained with the PIV 6 and the lower case letters with an asterisk are their homologous in the numerical results made

with OpenFOAM. Clearly, a similar parametric trend is observed for all the cases analyzed. These results show a significant difference because one approach is experimental and the other is a numerical approach. But the results are in acceptable ranges.

5.2. Liquid film velocity distribution

In the tests, the velocities of the film were variable, that is, it is never uniform due to the undulations. The velocity varies from zero on the walls to some maximum value at the interface [18] so average values of the velocity fields are presented.

The velocity fields in the numerical simulation on the left side of the figure 11 show that in the water injection plate there are small variations in speed between 1.8 and 1.2 kg/s. This is due to changes in angles in the inclined plate and its consequent changes in velocity profiles. Although these variations are not so great, the design of this injection head can still be improved. In addition, there is a thickening of the boundary layer of the liquid film upon leaving the head with its subsequent development. The water in direct contact with the solid walls of the chamber adheres to its surface due to the viscous effects and there is no slippage. This phenomenon is known as the non-slip condition. These changes are reflected in a balance between the thickness of the film and the amount of movement.
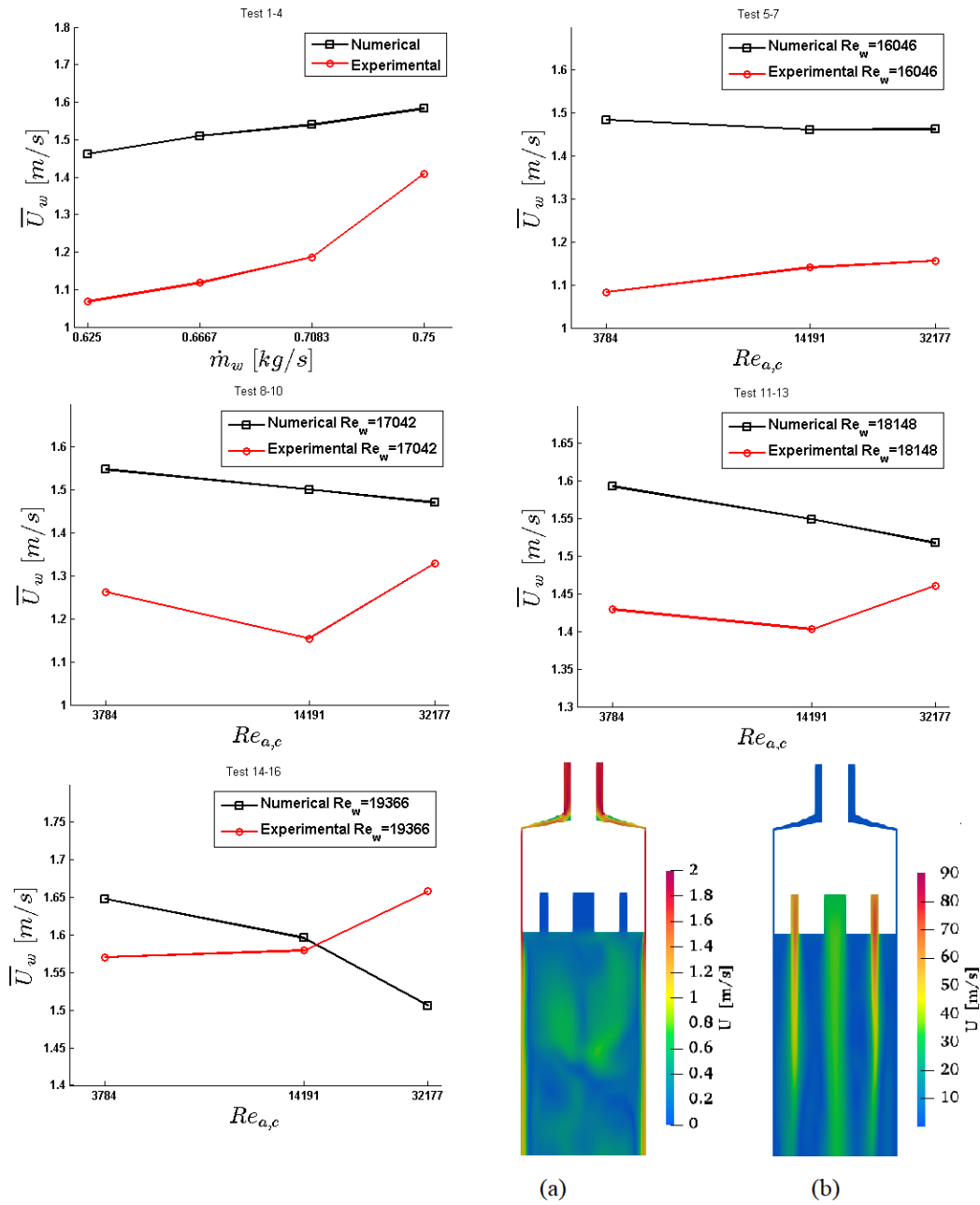
Figure 11: Average liquid film velocity according to the air and water Reynolds numbers. Velocity fields inside the chamber, from left to right: water film velocity without air injection for the test4, jet development for the test 16 at t=5s. Numerical results. Average liquid film velocity $\bar{U}_w$ according to the water mass flows $\dot{m}_w$. Tests 1-16.

On the right side of the figure 11 are also the diffusion of the perimeter jets according to the results of the previous section. It is clearly seen that the central jet has greater depth. The velocity is defined as the value of the averaged velocities along the cross section or annulus $\bar{U}_w$. In figure **??** tests 1-4 are shown, which correspond only to water injection. The black line are results derived from numerical simulation and the red line are the experimentally measured data. In the axis of the abscissa the injected water mass flow and in the axis of the ordinate the velocity of the liquid film.

It can be seen in the parametric tendency for both studies is to increase the velocity $\bar{U}_w$ in relation to the increase of the injected physical flow. For a lower water flow the velocity of the liquid film $\bar{U}_w$ is lower and increases with respect to the flows $\dot{m}_w$. In all cases with air injection, the variation in velocity is minimal. Although there is a difference in the numerical and experimental trend. It was observed in the experiment that the impact of speed is favorable on the stability of the film, eliminating disturbances. The behavior of the film is initially determined by the amount of water injected and its development is modified in each axial zone. According to the design objective of the injection head, for no experimental and numerical case was detachment or detachment of the film leaving the tube dry due to to the large differences in injection rates between the primary and secondary phases.

6. Summary

This work was an experimental and numerical study of the falling film flow in a chamber with an external diameter of 101.6 mm. The working fluids were water and air. The study was conducted under local atmospheric and adiabatic conditions. A non-intrusive PIV measurement system was used to measure the thickness and velocity of the cooling film in different axial areas. Experimental data was used to corroborate and validate the simulation model made in OpenFOAM, which uses the equations that govern the flow pattern. For all the tests carried out, the walls of the chamber of the $DHSG$ are kept protected by the liquid film at all times, although the nature of the flow is unstable, a design is obtained that maintains a stable film thickness. The parametric tendency of all cases is an undulatory phenomenon described by the axial variation of the interaction of the phases. The decrease in film thickness occurs when there is an increase in air injection and when the film is in the axial area furthest from the injection head. It is important to mention that the reduction in thickness is negligible when

compared with the results of other injection heads to generate the film. It is corroborated that, experimentally and numerically, increasing the mass flow of the air jets does not generate dry areas in the pipeline, therefore the injection head is in the design conditions for cooling $DHSG$. In conclusion the injection head is efficient and convenient to generate uniform and stable descending liquid cooling films. however, having disturbance waves there is likely to be interfacial atomization. Whereby is advisable to continue studying the system with other operating conditions. According to the nature of the phenomenon studied, it is recommended to do the experimental and numerical study for the characterization of the gas nucleus and thus lay the foundations for the beginning of the probable atomization of the movie. It is also possible to improve the geometry of the inclined plate with the technique called $Adjoint - Optimization$.

7. Acknowledgements

8. Nomenclature

Symbol	Description	Units
$A_{cs,annulus}$	Annulus cross section area	m^2
C_{rms}	Fluctuation scale	-
D_h	Hydraulic diameter	m
$D_{h,annulus}$	Annulus hydraulic diameter	m
D_t	External diameter	m
f_{surf}	Surface tension source term	$\frac{N}{m^3}$
g	Acceleration of gravity	$\frac{m}{s^2}$
I	Kronecker delta	-
k	Turbulent kinetic energy	$\frac{m^2}{s^2}$
Ma	Mach number	—
$\dot{m}_w$	Water mass flow	$\frac{kg}{s}$
$\dot{m}_a$	Air mass flow	$\frac{kg}{s}$
L_p	Pipe length	m
P	Pressure	Pa
P_h	Hydrostatic pressure	Pa
P_m	Manometric pressure	Pa
$Re_{w,f}$	Water Reynolds number for annulus	-
$Re_{a,c}$	Air Reynolds number for the central nozzle	-
$Re_{a,p}$	Air Reynolds number or the peripheral nozzles	-
R_1	Lower radius	m
R_2	Upper radius	m
S	Strain rate	-
t	Time	s
u	Velocity vector	$\frac{m}{s}$
u_{in}	Inlet velocity	$\frac{m}{s}$
u_r	Interface compression velocity vector	$\frac{m}{s}$
$v_{in,w}$	Water velocity in y direction	$\frac{m}{s}$
$v_{in,a}$	Air velocity in y direction	$\frac{m}{s}$
$v_{in,w,rand}$	Velocity value in the new instant after adding a random component	$\frac{m}{s}$
$v_{in,w,ref}$	Reference velocity value	$\frac{m}{s}$
s	Fluctuation scale	-
n	Time level	-
π	Pi	-

Greel Letter	Description	Units
α	Volume fraction of fluid	-
α_r	Fraction of new random velocity component added to previous time value	-
ϵ	Absolute roughness	m
δ	Liquid film thickness	m
ρ	Density of fluid	$\frac{kg}{m^3}$
μ	Dynamic viscosity of fluid	$\frac{kg}{ms}$
μ_{eff}	Effective kinematic viscosity	$\frac{kg}{ms}$
μ^{sgs}	Subgrid scale kinematic viscosity	$\frac{kg}{ms}$
μ_w	Water kinematic viscosity	$\frac{m}{s}$
ν_w	Water dynamic viscosity	$\frac{kg}{s}$
τ^{sgs}	Subgrid scale stress tensor	Pa
Δ	Filter cut-off width	-
σ	Surface tension	$\frac{N}{m}$

References

[1] Morison KR, Worth QAG, and O'dea NP. Minimum wetting and distribution rates in falling film evaporators. *Food Bioprod. Process.*, 84(4):302 – 310, 2006. Fouling, Cleaning and Disinfection in Food Processing.

[2] Frías-Esquivel J, González-Alatorre G, Díaz-Ovalle CO, Lesso-Arroyo R, and Ramos-Ojeda E. Hydrodynamic analysis of the falling-film formation in evaporators using cfd simulation. *Food Bioprod. Process.*, 101:56 – 67, 2017.

[3] Liucheng Y, Yifei W, Ziwei W, Zhenghua D, Guangsuo Y, and Fuchen W. Research of vertical falling film behavior in scrubbing-cooling tube. *Chem. Eng. Res. Des.*, 117:627 – 636, 2017.

[4] Knuth EL. *The mechanism of film cooling.* PhD thesis, California Institute of Technology, 1954.

[5] De la Cruz-Ávila M, Martínez-Espinosa E, Georgiy Polupan, and Vicente W. Numerical study of the effect of jet velocity on methane-oxygen confined inverse diffusion flame in a 4 lug-bolt array. *Energy*, 141:1629 – 1649, 2017.

[6] Borraz Jonapa LA. Estudio numérico de la estabilidad de una película de líquido descendente en el interior de un conducto circular. Master's thesis, Instituto Politécnico Nacional, Escuela Superior de Ingeniería Mecánica y Eléctrica, Unidad Culhuacán, 2015.

[7] De la Cruz-Ávila M. *Estudio numérico de la dispersión de gotas de agua en una llama difusiva turbulenta metano-oxigeno.* PhD thesis, Instituto Politécnico Nacional, Laboratorio de Ingeniería Térmica e Hidráulica Aplicada, 2017.

[8] Wang L, Wang Y, Guo Q, Yan L, and Yu G. Flow characteristics of vertical falling film in scrubbing-cooling pipe. *Huagong Xuebao/CIESC Journal*, 64:1959–1968, 06 2013.

[9] Larrainzar Solís EF. Estudio experimental de una película de líquido helicoidal descendente, interactuando con un jet de gases concurrentes usando piv. Master's thesis, Instituto Politécnico Nacional, Escuela Superior de Ingeniería Mecánica y Eléctrica, Unidad Culhuacán, 2016.

[10] Webb DR and Hewitt GF. Downwards co-current annular flow. *Int. J. Multiph. Flow*, 2(1):35 – 49, 1975.

[11] Larrainzar F, Moctezuma-Reyes J, Sánchez-Silva F, Carvajal-Mariscal I, and García-Demedices L. Evaluation of a vertical downward water film thickness using visualization and image recognition techniques. *Ingeniería Investigación y Tecnología*, 25:1–13, 2019.

[12] Fan W and Anglart H. varrhoturbvof: A new set of volume of fluid solvers for turbulent isothermal multiphase flows in openfoam. *Comput. Phys. Commun.*, 247:106876, 2020.

[13] Fernández-Oro JM. *Técnicas numéricas en Ingeniería de Fluidos*. Reverté, Barcelona, España, 2012.

[14] Neumann S, Dubberstein T, Chaves H, Kirmse C, and Schwarze R. Influencing parameter study on primary breakup of free falling steel melt jets using volume of fluid simulation. *Steel Res. Int.*, 87(8):1002–1013, 2016.

[15] Zamorano R. *Firefoam (CFD solver) validation in compartment fire scenario using high resolution data*. PhD thesis, Pontificia Universidad Católica de Chile, 2018.

[16] Le D, Labahn J, Beji T, Devaud CB, Weckman EJ, and Bounagui A. Assessment of the capabilities of firefoam to model large-scale fires in a well-confined and mechanically ventilated multi-compartment structure. *J. Fire Sci.*, 36(1):3 – 29, 2018.

[17] Brackbill JU, Kothe DB, and Zemach C. A continuum method for modeling surface tension. *J. Comput. Phys.*, 100(2):335 – 354, 1992.

[18] Azzopardi BJ. *Gas-Liquid Flows*. Begell House, Wallingford, U.K., 2006.

[19] Shine SR, Sunil Kumar S, and Suresh BN. Numerical study of wave disturbance in liquid cooling film. *Prop. Power R.*, 2(2):107 – 118, 2013.